PHYSICAL REVIEW RESEARCH **2**, 033436 (2020)

Domain walls in vertically vibrated monolayers of cylinders confined in annuli

Ariel Díaz-De Armas,[1] Martín Maza-Cuello,[2] Yuri Martínez-Ratón,[1,*] and Enrique Velasco[3,†]
[1] *Grupo Interdisciplinar de Sistemas Complejos (GISC), Departamento de Matemáticas, Escuela Politécnica Superior, Universidad Carlos III de Madrid, Avenida de la Universidad 30, E-28911 Leganés, Madrid, Spain*
[2] *Soft Matter Sciences and Engineering (SIMM), ESPCI Paris, PSL University, Sorbonne Universite, CNRS, F-75005 Paris, France*
[3] *Departamento de Física Teórica de la Materia Condensada, Instituto de Física de la Materia Condensada (IFIMAC) and Instituto de Ciencia de Materiales Nicolás Cabrera, Universidad Autónoma de Madrid, E-28049 Madrid, Spain*

(Received 19 May 2020; accepted 17 August 2020; published 17 September 2020)

Liquid-crystalline ordering in vertically vibrated granular monolayers of metallic rods confined in annuli of different sizes is examined. The annuli consist of circular cavities with a central circular obstruction. In the absence of the central obstruction, rods of low aspect ratio exhibit global tetratic order, except for the existence of four small defected regions which restore the tetratic symmetry broken by the circular confinement. However, very different configurations are observed in the annuli, with a complex structure consisting of alternating layered regions separated by tetratic domain walls. We use concepts of equilibrium elastic theory for liquid crystals and topology along with arguments based on dissipation mechanisms to qualitatively explain this behavior. The results show that selective confinement of vertically vibrated monolayers of rods could be used as a tool to study the creation and dynamics of various types of defects in ordered systems.

DOI: 10.1103/PhysRevResearch.2.033436

I. INTRODUCTION

The observation that quasi-two-dimensional monolayers of granular spherical particles can be excited by periodic motion, leading to pattern formation, has been investigated in the last decades [1–10]. A milestone in this field was the observation that some structural properties of a vibrated monolayer of spheres (in particular, crystallization), were similar to those of ordinary hard spheres in thermal equilibrium, a basic model to understand the structure of matter at the nano- and mesoscopic scales [11]. In some cases, these phenomena can be understood qualitatively by applying standard rules of equilibrium statistical mechanics [10,12]. Also, many nonequilibrium phenomena are observed in periodically agitated granular matter, e.g., the presence of solitons.

The inherently dissipative granular arrangements of anisotropic grains, when continually excited externally [13,14], also exhibit typically nonequilibrium effects [15–17]. Orientational order in 3D compaction experiments [18] as well as vortex formation in monolayers of rods that do not necessarily lie on the plane [19] have been investigated. But steady-state patterns in strictly 2D vibrated monolayers can be found by suitably choosing the control parameters of the external periodic drive, such as frequency and amplitude, imposed on the system. Vertically vibrated rods have recently been shown to exhibit spatial patterns that resemble liquid-crystalline phases with local and global nematic and tetratic ordering, usually seen in two-dimensional systems of thermal anisotropic particles [15–17,20–24].

Arguments borrowed from the elastic theory of liquid crystals (e.g., competing elastic bulk and surface energies) have been invoked to explain this phenomenology [22]. Indeed, it is tempting to describe the behavior in these systems in terms of entropic arguments based on volume exclusion, since forces between particles are absent except when they collide, and volume-filling concepts are certainly relevant. Recently, the phase diagram of equilibrium hard rectangles has been explored by Monte Carlo simulation and seen to exhibit many similarities, even quantitative, with the steady-state arrangements of granular rods confined in circular cavities [23]. We must remind ourselves that the behavior of hard particles driven by thermal fluctuations are exclusively controlled by entropy, i.e., by particle overlap statistics. This connection between thermal and nonthermal (granular) matter is intriguing, but only some partial ideas and basic relations can be advanced [25,26].

More recently, it has been shown that metallic rods of small aspect ratio may form global tetratic (i.e., fluid monolayers with fourfold orientational order) patterns inside circular cavities [20], along with the presence of what seem to be four point-defected regions, symmetrically located at the corners of a square inscribed in the circle [24,27]. The interpretation of these regions in terms of point topological charges that restore the broken fourfold symmetry of the tetratic director when confined to a circular cavity is appealing. It might indicate that, provided a continuum approximation is valid,

---

[*] yuri@math.uc3m.es
[†] enrique.velasco@uam.es

dissipative granular monolayers might respond to geometrical frustration in the same way as their thermal-equilibrium counterparts. This analogy has been exploited in Ref. [27] to extract an elastic constant that mediates the interaction between defects. The value of this constant turns out to be of the same order of magnitude as typical two-dimensional elastic constants of liquid crystals [27].

In this paper, we examine a vibrated monolayer confined in a topologically different geometry, namely, an annulus: a circular cavity with a central circular obstacle. Applying a topological argument, one should not expect the formation of point defects: regardless of the preferred orientation at the walls—-whether planar or perpendicular—a globally tetratic phase could accommodate inside the annulus without compromising the fourfold symmetry. Instead, steady-state configurations of the experimental system present a much more complex structure, with the presence of *domain walls* (i.e., extended regions) that separate regions with smectic liquid-crystalline ordering. These regions are similar to domain walls in materials where domains with different orientation of a nonscalar order parameter coexist (see, e.g., Ref. [28] where domain walls separating uniaxial nematic phases with different orientations were observed in circular cavities using Monte Carlo simulation). The breakdown of topological arguments may be perfectly reasonable in our nonequilibrium system. But it could also arise from the breakdown of the continuum approximation when the particle size is not negligible compared to the obstacle diameter.

The paper is organized as follows. In the following section, we present the experimental setup. Section III discusses the order parameters used to analyze the results. These are presented in Sec. IV. We conclude in Sec. V with a discussion of the results and present some conclusions.

II. EXPERIMENT

In the experiment, $\sim$2600–2800 cylinders made of nonmagnetic steel with length 4 mm and diameter 1 mm (aspect ratio $\kappa = L/D = 4$) are placed inside a cylindrical cavity of radius $R = 7$ cm ($R/L = 17.5$). The two planar, horizontal plates of the cavity are close enough so cylinders have a free height of 1.8 mm. Therefore, cylinders cannot pass each other and constitute an effective monolayer. The cavity is mechanically agitated at frequency $\nu = 90$ Hz using an electromagnetic shaker. The upper lid of the cavity is made of transparent plastic so a zenithal DSLR camera aligned along the cavity axis can record the time evolution of the particles. The cavity was carefully aligned with the horizontal by using a highly sensitive bubble level. The effective acceleration of the system can be measured in terms of the dimensionless acceleration $\Gamma = a_0\nu^2/g$, where a_0 is the amplitude of the vibration and g is the acceleration of gravity. In all the experiments performed, the effective acceleration was in the range $\Gamma \simeq 2$–3. The behavior of a vibrated monolayer may depend on the values of these two parameters [10]. Müller *et al.* [23] performed a detailed analysis of the effect of ν and Γ on a monolayer of plastic cylinders. They did not observe qualitative differences in the ordering properties in a wide range of values ($\nu = 35$–80 Hz and $\Gamma = 3$–17). For metallic cylinders, our experimental setup limits the possible values of Γ to the interval mentioned above but no changes in the results were observed in that interval. By contrast, the frequency was seen to be more critical and its value was chosen to avoid undesired nonequilibrium effects such as collective motion or creation of holes.

Particle identification (of position and orientation) is done using a MATLAB code implemented by the authors. The code locates the center of each particle and the angle between the long axis of the particle and a reference x axis. Distortion due to the curvature effects is negligible since the camera is at a long distance from the cavity and works at relatively long focal distance. Uniform illumination of the cavity is achieved by placing light diffusers surrounding the experiment. The identification software is very successful as typically a fraction $<1\%$ of the particles are not correctly identified. This fraction includes both single particles and pairs of close particles that cannot be discriminated. Some of the latter can be recovered by the identification algorithm using simple assumptions. In some exceptional cases, the fraction of misidentified particles can increase up to 3%. These experiments suffered from incorrect illumination or optical problems and were discarded for analysis.

With regard to the spatial resolution of particle positions and orientations, we estimate that the "optical" center of mass of a particle can generally be obtained with an accuracy of 1–2 pixels (in the CCD images a particle spans about 60 pixels in the long axis). The angular resolution in orientation is estimated to be $<4^\circ$. The software fits the apparent particles to ellipses, from which positions and orientations are inferred. Visual inspection of ellipses superimposed on actual particles leads to the above estimates. The resolution in position is $\sim 0.002R$, much less than the resolution in radial direction of the histograms shown in Sec. IV. Therefore, we believe the results for radial histograms and orientational order parameters are not affected by the accuracy in particle identification, neither in position nor orientation.

In each experiment, the protocol used was the following. First, the initial configuration is prepared by hand: the upper lid of the cavity is removed and cylinders are placed on the lower surface, avoiding any overlaps. Then the cavity is covered by the lid. The packing fraction η, i.e., the fraction of effective projected area covered by the particles with respect to the total area of the cavity, is estimated by taking a picture of the static system and using the identification software. In case the target density is not achieved, particles are removed or added according to the difference between actual and target packing fractions. Images are taken typically every 15 s, and experiments are run for several hours. In all cases, the system gets readily ordered after the experiment is started, but a completely stable (in the steady-state sense) regime is attained only after an hour or more.

III. ORDER PARAMETERS

Similar to previous work on a similar experimental setup [17], we obtained different types of particle arrangements, depending mainly on the packing density of the system: I (isotropic) at low packing fraction, where particles are disordered in both orientations and positions; N_t (tetratic) at intermediate packing fraction, where particles show fluid behavior but are oriented on average along two equivalent, perpendicular directions; and S (smectic) at high packing fraction, with particles forming fluid layers.

For the definition of order parameters, the local director $\hat{\boldsymbol{n}}$ on each particle is required. This is obtained by first defining a circular region C of radius $\xi = 4L$ centered at each particle and then calculating the 2×2 tensor,

$$Q = \langle 2\hat{\boldsymbol{e}}_k\hat{\boldsymbol{e}}_k^T - I\rangle = \frac{1}{M}\sum_{k=1}^{M}\left(2\hat{\boldsymbol{e}}_k\hat{\boldsymbol{e}}_k^T - I\right), \tag{1}$$

which defines the average $\langle\cdots\rangle$. Here $\hat{\boldsymbol{e}}_k$ is the unit column vector along the long axis of particle k, the sum in k extends over all M particles whose centers of mass are contained in region C, and I is the 2×2 identity matrix. The eigenvector of Q associated with the largest eigenvalue defines the local director $\hat{\boldsymbol{n}}$ on the particle.

The identification of configurations with different symmetries (I, N_u, N_t or S) can be done by means of a number of order parameters. In this case, we define three order parameters. On the one hand, two orientational order parameters:

$$q_n = \langle \cos n\theta\rangle \quad \text{with} \quad n = 2, 4, \tag{2}$$

which probe two- and fourfold symmetries, respectively, uniaxial and tetratic symmetries. θ is the angle between the long axis of a particle and the local alignment direction $\hat{\boldsymbol{n}}$ (local director). On the other hand, we define the smectic order parameter as

$$q_s = \langle e^{i\boldsymbol{q}\cdot\boldsymbol{r}}\rangle. \tag{3}$$

Here $\boldsymbol{r}$ is the position of a particle and $\boldsymbol{q}$ a wave vector compatible with the cylinder length (in fact, a little larger to allow for smectic layer fluctuations). Both these vectors are referred to the frame defined by the local director. One essential characteristic of our order-parameter-based description is that q_2, q_4, q_s are not defined as local fields at a point $\boldsymbol{r}$, but on each particle. This is similar to the Eulerian versus Lagrangian views of the flow field of a fluid. The advantage of this approach is that visualisation of order in separate configurations is much easier. On the other hand, our Lagrangian approach also allows us to obtain average values over the whole cavity in the steady state.

Local configurations can be identified as follows:

(i) I: $q_2 \sim q_4 \simeq 0$ and $q_s \simeq 0$
(ii) N_u: $q_2 \simeq q_4$ and $q_s \simeq 0$
(iii) N_t: $q_2 \ll q_4$ and $q_s \simeq 0$
(iv) S: $q_2 \gtrsim q_4$ and $q_s > 0$

The N_u (uniaxial nematic) phase is not observed in our experiments, as the particle aspect ratio is too small (others reasons may also explain this finding, see Ref. [24]). An essential property of the steady states of this system is that, except at low packing fractions (a regime which is not explored in detail in the present paper), the values of the order parameters are not the same, not even of the same order, in different regions of the cavity. Note that, in our experiments for $\kappa = 4$, extended uniaxial nematic configurations are not formed for any value of aspect ratio.

The local order parameters represent a powerful tool to identify the ordering in the cavity in space and also in time. In practice, we analyzed all images taken by the acquisition system, identifying particles and calculating the three order parameters on each particle. We produced three sequences of images, color-coded according to the value of $q_2,\ q_4,\ q_s$. The processed images were piled up to produce videos, which are very helpful to visualize the ordering dynamics, particle motion, and evolution of defected structures in the system.

Typically, in the course of the experiments, the system is prone to developing a global rotation, which closely corresponds to a rigid rotation. This rotation follows a chaotic temporal pattern, both in amplitude and direction. The rotation can be eliminated from the analysis by defining an instantaneous reference frame where the average azimuthal position of the defects is constant. Motion with respect to this frame contains the inherent defect fluctuations. In the remainder of this paper, it should be understood that all results are defined in this average frame.

IV. RESULTS

Several experiments with different packing fractions in each case were considered. However, we concentrate on comparing cases with approximately the same packing fractions and different obstacle sizes. The reason is that the interesting density window is relatively narrow: (i) for $\eta \lesssim 0.70$, the tetratic phase is not well developed in the cavity, and therefore defects are not well-defined entities along the whole time span of the experiments; and (ii) systems with $\eta > 0.75$ are very difficult to prepare manually due to the high density. Therefore, we focus on systems with $\eta \simeq 0.75$, for which a well-structured tetratic configuration is developed.

We have investigated four different systems: no obstacle, 0, small obstacle, 1 (1 cm in diameter), intermediate obstacle, 2 (2 cm in diameter), and large obstacle, 4 (4 cm in diameter). The main experimental results for packing fraction fixed to $\eta \simeq 0.74$ are shown in Fig. 1 (specifically, packing-fraction values were, respectively, 0.735, 0.756, 0.744, and 0.743). The rows represent the different order-parameter fields $q_2,\ q_4,\ q_s$ while the columns represents different obstacle sizes $= \{0, 1, 2, 4\}$. The figure show instantaneous configurations of particles, color-coded according to the values of q_α ($\alpha = 2, 4, s$).

A. No obstacle: Circular cavity

This system was studied previously [23,24,27], and is here reanalyzed as a reference case (note that the experiment was slightly redesigned with respect to that of Refs. [24,27]; in particular, the cavity is slightly bigger). In this section, we also define some other quantities that will be used in the other cases.

Figure 1, column 0, shows a typical configuration in the steady state. All three order parameters are shown. The high value of the q_4 order parameter in a large fraction of the area, together with the low values of q_2 and q_s, points to the formation of a large region of tetratic symmetry occupying a very large area of the whole cavity. Figure 2(a) shows a representative example of particles in a tetratic configuration.

In addition, there are four regions where all three order parameters are depleted, corresponding to particles with orientational disorder. These regions may be interpreted, using

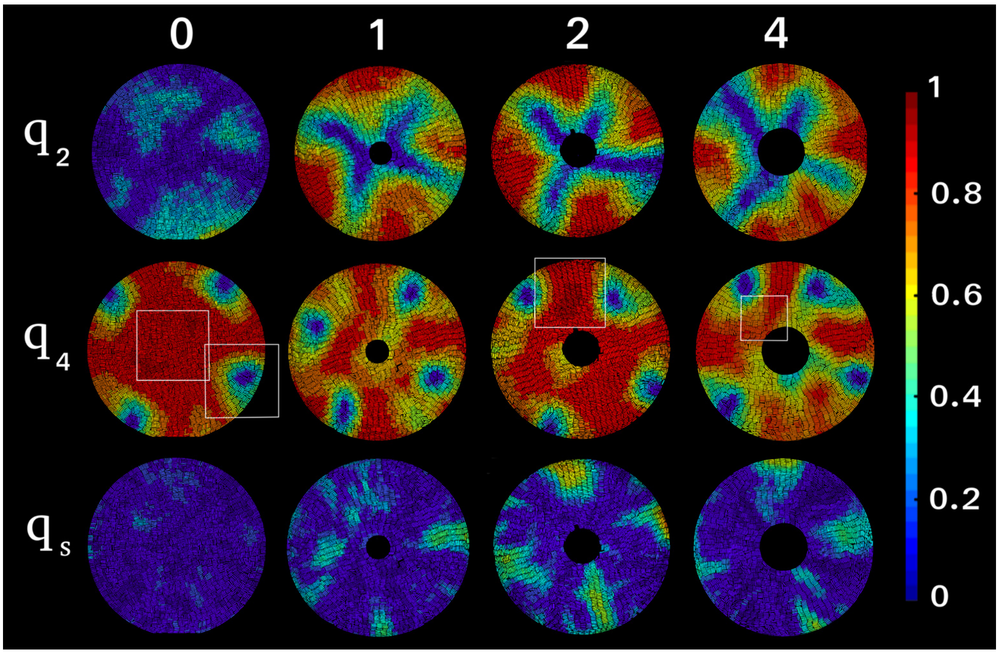

FIG. 1. Values of the q_2 (uniaxial), q_4 (tetratic), and q_s (smectic) order parameters on each particle, and for the four situations investigated in this paper. 0: no obstacle; 1: small obstacle; 2: intermediate obstacle; and 4: large obstacle. In each case, the configuration has been chosen more or less at random during the course of the respective experiments. Different color codes for q_2, q_4, and for q_s are shown in vertical bars. In all experiments, particles had $\kappa = 4$ and packing fraction was set to $\eta \simeq 0.75$. Values for the other parameters were taken as mentioned in Sec. III. Boxes in panels q_4-0, q_4-2, and q_4-4 are shown at larger scale in Figs. 2(a), 2(b), 2(d), and 2(e), respectively.

topological arguments, as "point" defects which restore the global symmetry of the tetratic phase broken by the circular cavity, which is incompatible with the fourfold symmetry of the tetratic phase. The defects are pointlike in the sense that their associated depleted region (the "core" of the defect) has a finite area. An example of particle configurations in one such region is shown in Fig. 2(b). A calculation based on elastic theory, Fig. 2(c), confirms that the director field in these regions corresponds to a defect with winding number $+1/4$ and topological charge $+1$. The four defects are located at the corners of a square. Using the language of elastic theory, this tetratic configuration with four defects still forces some distortion of the local tetratic directors close to the walls between contiguous defects. But the distortion is assimilated by the system through the accumulation of elastic free energy, without producing additional defective regions.

Defects were identified by first selecting those particles with an order parameter $q_4 < 0.4$. A given particle is taken to belong to a particular cluster if its center-to-center distance to at least one particle of the cluster is less than one particle length. This criterion is sufficient to isolate separate clusters in the system which are potential candidates for the pointlike defects. On most occasions, only four such clusters are found, as can be seen in Fig. 1. The center of mass of each cluster is taken as the defect location.

The position of the four defects fluctuates in time but they always stay close to the cavity wall. In Ref. [27], we argued that this can be explained using arguments from equilibrium elastic theory: Defects interact repulsively, via a logarithmic interaction which is mediated by the stiffness coefficient K of the intervening, tetratic phase. The value of K can be estimated from defect fluctuations and, when conveniently scaled, is of the same order as in two-dimensional liquid crystals.

Note that in these experiments particles remain in a "fluid" tetratic state with high mobility, and that smectic fluctuations only appear rarely and decay very quickly. This is important

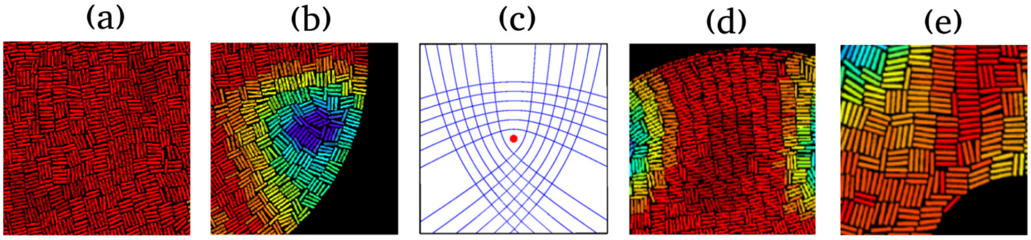

FIG. 2. (a) Detail of panel q_4-0 of Fig. 1 showing strong N_t ordering. (b) Detail of panel q_4-0 of Fig. 1 showing one of the defects. (c) Orthogonal family of curves as obtained from elastic theory representing the tetratic director field around a defect (circle) with winding number $+1/4$. (d) Detail of panel q_4-2 of Fig. 1 showing a region with strong smectic ordering. (e) Detail of panel q_4-4 of Fig. 1, showing a region with tetratic ordering in a bridge connecting a point defect with the inner boundary.

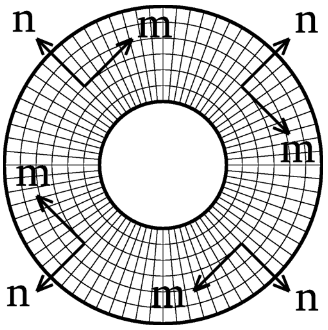

FIG. 3. Schematic of the director field of a tetratic configuration inside an annulus. The local orientation of the directors $\hat{\boldsymbol{n}}$ and $\hat{\boldsymbol{m}}$ is indicated at four particular locations. The system is invariant under the local symmetry operations $\hat{\boldsymbol{n}} \to -\hat{\boldsymbol{n}}$ and $\hat{\boldsymbol{m}} \to -\hat{\boldsymbol{m}}$. Continuous lines represent director field lines.

because, as we will discuss shortly, the annular geometry do stabilize the formation of smectic domains.

B. Annuli

Having reviewed the no-obstacle cavity, we now turn to the annular cavities. As discussed in Sec. V, the topology of the annulus is different from that of the disk and in fact fully compatible with the tetratic four-fold symmetry. Therefore, topology would not require the presence of defects in the cavity but simply a distorted tetratic phase, with the two locally perpendicular directors $\hat{\boldsymbol{n}}$ and $\hat{\boldsymbol{m}}$. In the language of continuum liquid crystals, these directors should exhibit two distortion modes: splay (affecting the $\hat{\boldsymbol{n}}$ director, the one pointing in the radial direction) and bend (affecting $\hat{\boldsymbol{m}}$, the one along the azimuthal direction). Note that the system is invariant under the symmetry operations $\hat{\boldsymbol{n}} \to -\hat{\boldsymbol{n}}$ and $\hat{\boldsymbol{m}} \to -\hat{\boldsymbol{m}}$. See Fig. 3 for a schematic representation of distorted tetratic directors inside an annulus; distortion avoids the excitation of defects because the condition of parallel orientation at the boundary is perfectly fulfilled without compromising the global symmetry of the system.

Topological arguments were successful in explaining the global properties of the cavity in the case where no obstacle is present. However, the results for the annuli, presented in Fig. 1, are considerably more complicated than expected. Again, typical particle configurations with color-coded values of the order parameters superimposed are shown. Visual comparison with the reference, no-obstacle case may help reveal different phenomena induced by the obstacle. The column labeled 1 corresponds to the small obstacle. On first sight, from the q_4 map, one may conclude that the four defects of the obstacle-free configurations are still present. Indeed, from the q_4 maps for the other obstacle sizes, columns 2 and 4, we can draw the same conclusion: spatially limited regions with a depleted tetratic order parameter are clearly excited. The arguments taken from topology are apparently not valid.

The apparent similarity between configurations in circular and annular cavities might be explained by regarding the obstacle as a perturbation to the tetratic field. The obstacle would weaken the long-range interaction between defects, especially second-neighbor ones (those located along the diagonal of the square defined by the four defects). As a consequence, we might expect to see larger fluctuations in the defect positions: excursions of the defects away from the wall and into the bulk of the cavity will be longer, while the integrity of the defects as pointlike particles will remain intact. This effect is not very clear when comparing the q_4 maps as we move from experiment 1 to experiment 4, but will be quantified and confirmed later by examining the distribution and shape of the defects.

However, a closer look at the other order-parameter maps gives a much more clear interpretation and reveals a complex structure in the annular cases. Let us first consider the q_2 map. In the obstacle-free case, it is low, except for localized, short-lived, and rapidly decaying regions, corresponding to excitations of the local uniaxial order associated with the smectic fluctuations alluded to above. By contrast, in the annular experiments, the q_2 maps exhibit very apparent and persistent structures with a high value. It turns out that in the regions where the q_2 order parameter is high, the smectic order parameter q_s is also high. These regions are long-lived, genuine smectic domains (note that layers tend to bend and present disclinations, which are typical of smectic order. As a result of local averaging, the order parameter q_s turns out to be generally low over smectic regions even though, as clearly seen in the q_s maps of Fig. 1, strong layered structures are quite apparent). In these smectic regions, the q_4 order parameter is also high, as expected. In Fig. 2(d), a detail of panel q_4-2 of Fig. 1 is shown, representing a region with high values of both q_2 and q_s. Smectic ordering of particles arranged side by side, forming a layered texture, is clearly seen.

Further examination of the maps in Fig. 1 reveal the existence of regions where the q_2 order parameter is depleted. These regions can be identified by their cross-shaped structure in panels q_2-1, q_2-2, and q_2-4. An interesting observation is that these regions, with low q_2, are *spatially complementary* to the smectic regions with high q_2, both alternating periodically in the azimuthal direction. These fan-shaped "bridges" are oriented at relative angles of 90° and connect the wall of the container with the wall of the central obstacle. Figure 2(e) shows a detail of one of such bridges in panel q_4-4 of Fig. 1. In these regions, q_4 is high whereas q_2 is low: this corresponds to strong tetratic ordering, meaning that the bridges are tetratic domain walls that separate neighboring smectic domains.

But the structure of the tetratic domain walls is complex. Close to the outer cavity wall, both q_2 and q_4 are depleted, indicating that particles are orientationally disordered (isotropic region); this is reminiscent of the no-obstacle situation and, in fact, q_4 maps reveal the presence of pointlike defects. Their structure is identical to that in the no-obstacle case, Fig. 2(b). As we move away from the outer wall, toward the central obstacle and along the radial direction, the q_2 order parameter remains depleted. Therefore, tetratic domain walls actually contain an embedded point defect close to the outer wall. The arc at the inner wall is short enough that particles can easily accommodate in a tetratic configuration close to the obstacle, despite the large curvature (only a small length of the obstacle wall is covered by particles with tetratic ordering).

In the remainder of this section we present further results that quantify the overall structure of defects in the cavities, their spatial distribution, and shape. In Ref. [27], it proved

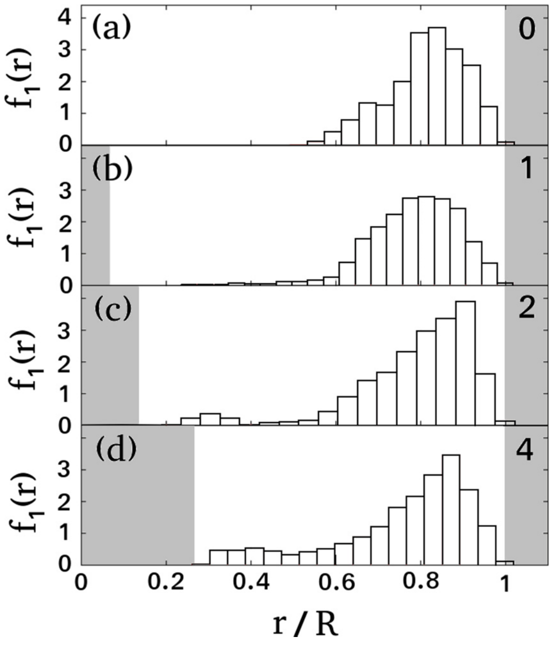

FIG. 4. Radial distribution of defect positions for (a) no obstacle, (b) obstacles of diameter $d = 1$, (c) $d = 2$, and (d) $d = 4$. Shaded areas indicate regions that cannot be explored by the defects (central obstacle at left and region outside cavity at right).

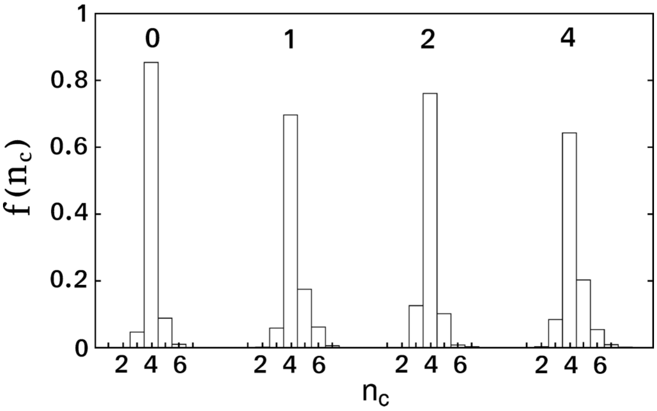

FIG. 5. Histogram of the number of defects, n_c inside the cavity (for clusters larger than five rods) for all the cases explored. Note that the horizontal axis has been displaced in each case. Labels on the top indicate the diameter of the obstacle in cm.

useful to characterize the motion of the defects in terms of distribution functions. We also adopt this approach here and define $f_1(r)$, the *radial function*, which gives the spatial distribution of the defects with respect to their distance r from the center of the cavity. This function is averaged over time and over the four defects. r is conveniently scaled by the cavity radius R. Since defects are mostly located close to the cavity wall, one expects that $f_1(r)$ presents a maximum at a radial distance $r/R \lesssim 1$. Analysis of this function provides information on the excursions of defects inside the cavity and the spatial fluctuations.

The histogram of $f_1(r)$ is shown in Fig. 4. A total of ca. 1000 images were used to compute the histogram. In this (and, in fact, in all the other histograms shown in the following), error bars were not included since statistics are rather poor. The reason is that radial histograms demand at least 20 bins to actually see significant trends, and the number of data points inside each bin is not actually high, especially close to the cavity center. As a consequence, local standard-deviation values may be of the same order as the local mean. We believe this is not a serious problem since the overall behavior seems to be consistent. Figure 4(a) shows the reference case, with no obstacle. We can see that the distribution is quite broad, spanning approximately half the available radial distance. As indicated in Ref. [27] (which corresponds to a different experiment on a slightly smaller cavity), the radial distribution seems to be bimodal, with two typical distances: one at $r/R = 0.85$ and another at 0.65. The bimodality might be caused by the layered structure formed by the rods close to the wall, which pushes the defects away from the wall at a distance that depends on the orientation of the rods and the number of layers [27]. The opposing effect, coming from defect repulsion, competes with the wall repulsion and may give rise to a bistable position. Although the surface structure at the wall has not been investigated carefully, it is observed that it is quite dynamic. In Fig. 4(b), we plot the results for the situation with the small obstacle. In this case, the bimodality disappears and the distribution is broader, exhibiting a long tail toward the cavity center which indicates the tendency of the point defects to explore larger radial distances within the tetratic domain walls. The effect is more pronounced as the obstacle becomes bigger.

Another interesting quantity is the histogram of the number of defects in the cavity, Fig. 5. Only defects formed by clusters of more than five particles have been included in the calculation to avoid clusters that simply represent local fluctuations and are not related to fully developed defects that participate in the global interactions inside the cavity. Clearly, in the no-obstacle case, in most configurations one finds four defects, and only a few times are more or less than four defects excited inside the cavity. However, when the obstacle is present, it is more likely to find more than four defects, which means that defect interactions have been weakened and the restrictions imposed by topology are relaxed.

We have also calculated the distribution of the size of the defects (number of rods belonging to the defect cluster). Figure 6 shows the distribution of clusters with a size larger than five rods. The peaks of the distribution in the circular and annular cavities occur at sizes that increase slightly, but the distribution gets broader as the obstacle becomes larger. From this feature, it can be inferred that defects are slightly larger on average when the obstacle perturbs the tetratic field.

Also of importance is the shape of the defects. When there is no obstacle, defects are not completely circular because they are close to the wall and therefore in an anisotropic environment. The presence of a central obstacle amplifies this effect, as we presently show. In Fig. 7, the distribution in a and b (with $a > b$), the two principal lengths of all clusters larger than five rods, are shown. Both lengths are normalized with the radius of the cavity R. These lengths have been obtained by diagonalizing the moment of inertia tensor calculated from all rods that belong to a given cluster (assigning a unit mass to the rods), and then taking the square root. We can see that,

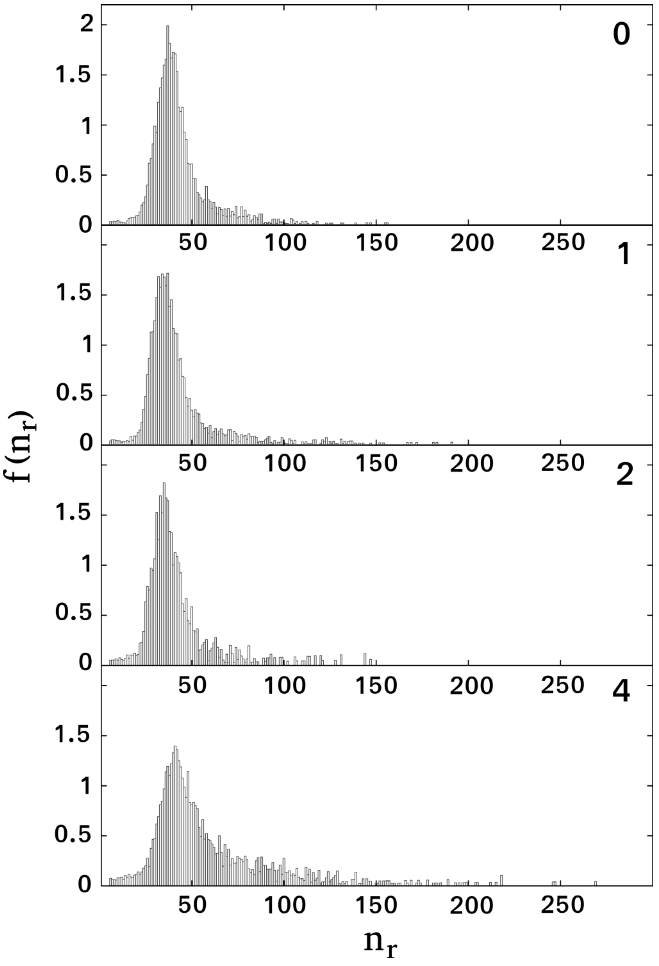

FIG. 6. Distribution of number of rods n_r in clusters containing more than five rods. From top to bottom: no obstacle, and obstacles of small, intermediate, and large size. Labels indicate the diameter of the obstacle in cm.

as the size of the central obstacle increases, the two lengths get more different, meaning that the defects become more elongated. From the corresponding eigenvectors, it is inferred that the direction along which the long size of the cluster points changes from azimuthal (no obstacle) to radial (toward the cavity center, in the case of the 2 and 4 obstacles; these results are not shown). One obvious explanation is that point defects are now confined into thin domain walls, becoming elongated along the radial direction.

In the case of the large obstacle, the distribution associated to the long axis gets broader and in fact the probability that the defect spans the whole radial distance (from the obstacle to the wall, meaning that the whole domain wall becomes disordered) increases dramatically. By contrast, the short axis remains more localized. This means that sometimes the defects connect the inner and the outer boundaries of the cavity by a bridge. An example of this behavior, which becomes more evident as the size of the central obstacle becomes larger, is shown later.

Figure 8 shows the distribution of the oblateness of defects, $\epsilon = 1 - b/a$. As the obstacle gets larger, the distribution in ϵ becomes broader, with the mean value of ϵ increasing from

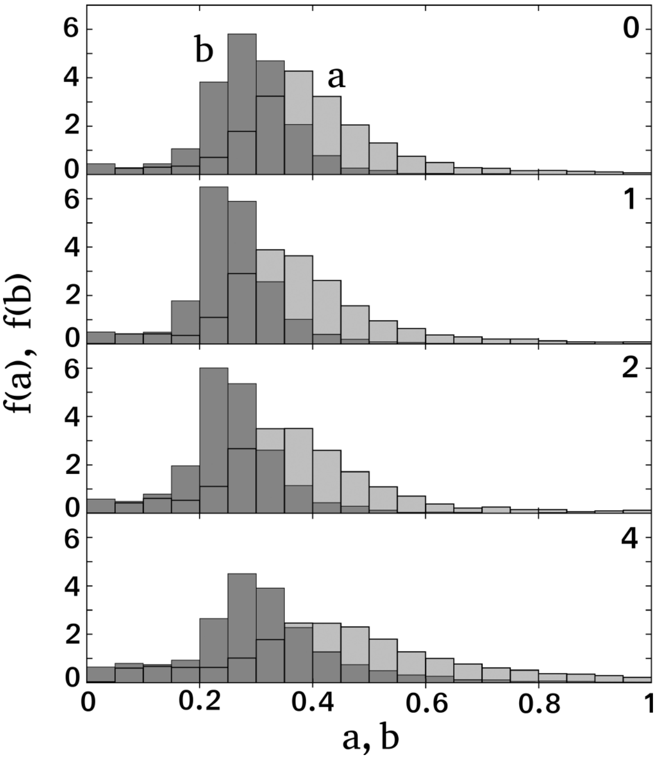

FIG. 7. Distribution of principal lengths of the defects a and b. From top to bottom: no obstacle, and obstacles of small, intermediate and large size. Light grey: long axis; dark grey: short axis. Labels indicate the diameter of the obstacle in cm.

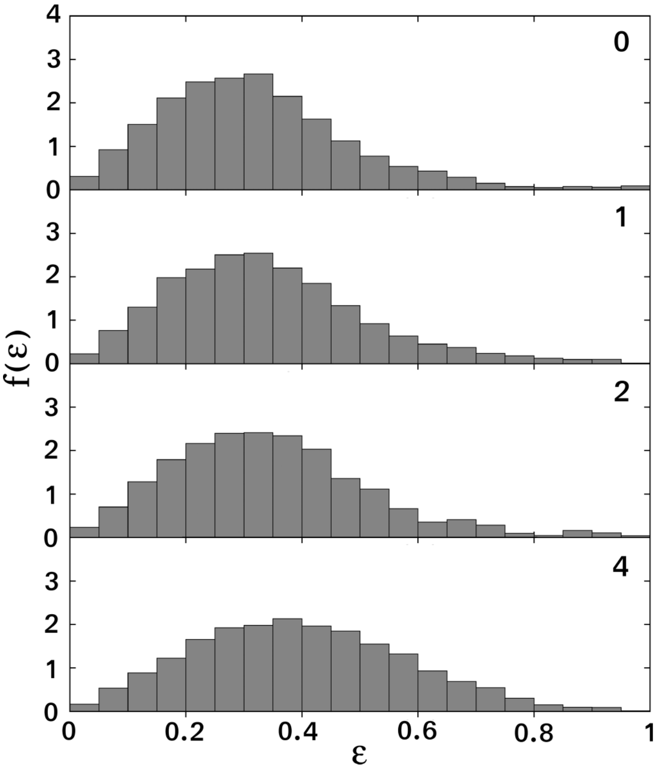

FIG. 8. Distribution of the oblateness $\epsilon = 1 - b/a$ of defects. Labels indicate the diameter of the obstacle in cm.

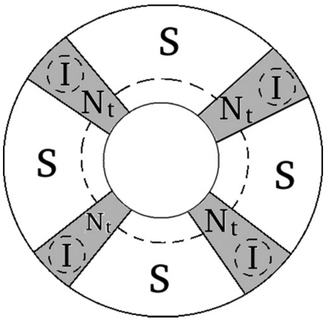

FIG. 9. Schematic diagram showing the structure of domain walls (shaded) in the circular annulus. Smectic (S) regions are separated by domain walls consisting of tetratic (N_t) regions and isotropic (I), defective regions. Dashed lines separate regions close to the inner wall where the type of order, either smectic or tetratic, depends on the obstacle size.

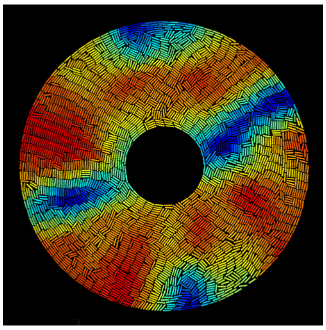

FIG. 10. q_4 order parameter field of a particular configuration of one of the experiments involving the larger obstacle. Two of the defects are localized, while the other two are extended and connect the inner and outer walls of the cavity.

~0.32 to ~0.40. Figure 9 is a schematic diagram showing the structure of the domain walls in the annulus. S regions are separated by domain walls consisting of N_t and I, defective regions. This structure can be deduced from the order-parameter maps of Fig. 1. The pointlike defects are reminiscent of the structure in an obstacle-free cavity. It seems that pointlike defects are easily formed due to the high tendency of the system to develop orientational order, either uniaxial (smectic) or tetratic. In turn, tetratic regions are developed in the radial segment of the pointlike defects to avoid distortion of the smectic layers. Note that the regions close to the obstacle wall in each smectic domain usually tend to be tetratic, especially in the case of the smaller obstacles since curvature is too large to support bent smectic layers (see Fig. 1).

Despite the presence of the obstacle, which forces the particles to dramatically rearrange into a complex structure, the dynamics can still be interpreted in terms of point defects (isotropic regions) that interact at distance. Clearly the obstacle will tend to weaken the long-range interaction, but the now smectic (instead of tetratic) regions between nearest-neighbor defects will certainly reinforce the repulsive interaction. The reason is that in this case the interaction is mostly mediated by smectic layers, in the direction perpendicular to the layers. Since smectic phases have a small compressibility and, consequently, a large stiffness coefficient associated to the layer periodicity, the amplitude of the logarithmic interaction will probably be very large. Defects still stay close to the cavity wall because of the overall strong interdefect repulsion.

Results from Figs. 4–8 are summarized in Table I, where mean and standard deviations for the quantities represented in the figures are given. The collected data confirm the scenario discussed in the previous paragraphs, and can be rationalized as follows. The mean number of clusters (defects), $\overline{n}_c$, slightly increases with obstacle diameter, while the mean number of rods that belong to clusters, $\overline{n}_r$, remains approximately the same, except for the largest obstacle which exhibits much larger clusters. Al,so the centers of mass of clusters $\overline{r/R}$ have a weak tendency to drift toward the cavity center. Finally, the mean oblateness of defects, $\overline{\epsilon}$, increases monotonically with obstacle size, confirming the tendency of defects to become more elongated along the the radial direction. An example of this trend is given in Fig. 10, which shows the q_4 order parameter of a configuration where two of the defects exhibit a large shape fluctuation consisting of elongated structures in the radial direction. In this case, the fluctuation is so strong that the defects connect the inner and outer cavity boundaries. This type of configuration, however, represents a small fraction of the total. In general, the strongest fluctuations in all measured magnitudes are found in the system with the larger obstacle, which is also reflected in the values of standard deviation collected in the table.

TABLE I. Summary of mean and standard deviation values obtained from the histograms shown in Figs. 4–8 for the four experiments analyzed. In each case, mean and standard deviations are given. The meaning of the quantities is as follows. $\overline{n}_c$: mean number of clusters in the cavity. $\overline{n}_r$: mean number of cylinders in clusters. $\overline{r/R}$: mean radial position of defects from the cavity center in units of the cavity radius. $\overline{a}$: mean value of major axis of defects. $\overline{b}$: mean value of minor axis of defects. $\overline{\epsilon}$: mean value of oblateness parameters of defects.

	0	1	2	4
$\overline{n}_c$	3.738 ± 0.593	3.890 ± 0.873	3.996 ± 0.510	4.246 ± 0.727
$\overline{n}_r$	42.642 ± 16.973	42.745 ± 22.674	41.550 ± 19.840	58.927 ± 35.026
$\overline{r/R}$	0.821 ± 0.107	0.780 ± 0.115	0.783 ± 0.147	0.755 ± 0.164
$\overline{a}$	0.407 ± 0.141	0.382 ± 0.145	0.385 ± 0.154	0.458 ± 0.197
$\overline{b}$	0.283 ± 0.086	0.254 ± 0.081	0.254 ± 0.092	0.305 ± 0.133
$\overline{\epsilon}$	0.319 ± 0.163	0.338 ± 0.169	0.347 ± 0.173	0.399 ± 0.181

V. DISCUSSION AND CONCLUSIONS

The theoretical interpretion of the results presented in the previous section is not easy, since at present there is no theoretical framework available for dense vibrated monolayers of anisotropic granular particles. Therefore, we can only speculate based on equilibrium concepts and other arguments rooted on dissipation mechanisms.

We start with the topological arguments. Galanis *et al.* [22] have assumed continuum elastic theory and concepts such as surface anchoring in their analysis of vibration experiments on long granular needles confined in circular cavities, where only uniaxial nematic ordering is possible. Our results for a similar system with tetratic symmetry (no-obstacle case) seem to also follow these concepts. In fact, the vibration experiments on annular cavities, presented in the previous sections, were motivated by the radical changes predicted by topology with respect to circular cavities: four pointlike defects in the latter and no defects in the annuli. The notion is based on the so-called *geometrical frustration*: In the circular cavity, due to the boundary conditions imposed and assuming strong anchoring conditions (either planar or homeotropic), bulk fourfold local orientational order (C_4 symmetry) cannot propagate globally because of the circular geometry of the cavity. Continuity of the tetratic field must necessarily be restored by creating defects.

This concept can be quantified using the Euler theorem of topology applied to the experimentally obtained tetratic field [29]. In the present context, the theorem states that the total topological charge of the system must satisfy the equation $\sum_i Q_i = p\chi$, where p is the symmetry order of the phase (in the case of the tetratic, $p = 4$), while χ is the Euler characteristic of the volume. In the case of a circular cavity consisting of a disk, $\chi = 1$. Q_i is the topological charge of each individual defect present in the volume, a number that reflects the symmetry of the order parameter around the defect. The Euler theorem gives the total charge of the system, not the number or topological charge of the defects present. These properties depend on other considerations based on the competition between free-energy contributions of different origin: bulk, wall, elastic, and defect core energies. In any case, the system will minimize the free energy by choosing the minimum number of defects that can restore the broken symmetry induced by the confining boundary. In a circular cavity, the presence of four defects restores the symmetry broken by the circular geometry of the cavity since the total charge $+4$ (four defects of charge $+1$) satisfies the constraint imposed by the Euler theorem for a medium with C_4 symmetry.

For the annular geometry, the Euler characteristic is $\chi = 0$, meaning that the total topological charge inside the volume should be zero. In fact, the integrity of the director field can be maintained, without the presence of any singularities, by distorting the field around the central obstacle without ever creating any conflict with the wall contour. The symmetry of the tetratic field is not compromised in this case because no geometrical frustration should exist.

Our results for the annular cavities do not conform to the topological requirements. As soon as the tetratic field is disrupted by the presence of a central obstacle, regardless of its size, the system is divided up into regions periodically arranged in the azimuthal direction: (i) regions with smectic order and (ii) tetratic domain walls containing pointlike defects. The latter are identical to the defects observed in the systems with no central obstacle. These structures tend to migrate slightly toward the central obstacle and their shape becomes more elongated, due to their more anisotropic environment, with respect to the obstacle-free case.

That the steady-state structures in the annuli are not in accordance with the predictions from continuum elastic theory and topology may not be surprising, as we are dealing with nonequilibrium systems governed by dissipation. As discussed in Ref. [24], vibrated monolayers show a strong tendency to form large clusters of particles arranged side by side, and consequently local smectic fluctuations are frequent. This clustering effect can be explained by local energy disspation due to particle collisions. But large layered structures are short lived because layers are easily disrupted by the excitation of local vorticity. This is indeed observed in our obstacle-free experiments. However, the presence of a central obstacle in the cavity suppresses vorticity and stabilizes large smectic regions. If dissipation-induced clustering is behind the formation of stable smectic structures, monolayers of rods in thermal equilibrium (as, e.g., in equilibrium particle simulations) should behave in a radically different manner.

However, dissipation may not be the only factor. The reduced size of the cavity, and in particular of the central obstacle, compared with the length of the cylinders, may also be important as the continuum approximation based on a continuous, smoothly distorted tetratic field may not be valid. If the size of the obstacle is of the order of a few particle lengths, arguments based on topology make no sense and other considerations are needed to explain the phenomenology. To emphasise this point more clearly, let us recall the typical lengths of our system: L, the particle length; R, the radius of the cavity; and R_{obs}, the radius of the central obstacle. The continuous field assumption rests on the conditions $R \gg L$ and $R_{\mathrm{obs}} \gg L$. While the first condition is probably fulfilled in our experiments, which have $R/L = 17.5$ (and the success of topological arguments in the no-obstacle case strongly supports this), in the case of the small obstacle we have $R_{\mathrm{obs}} = 0.5$ cm and consequently $R_{\mathrm{obs}}/L = 1.25$. The perimeter of the central obstacle is covered by only $\sim 2\pi R_{\mathrm{obs}}/L \sim 8$ particles forming an octagon. Certainly, the continuum approximation breaks down, and topological arguments may not be valid in this case. For the other obstacles, we have $R_{\mathrm{obs}}/L = 2.5$ and 5, still too small for the continuum approximation to be valid.

If the structures observed are the result of a nonequilibrium effect, there is no *a priori* reason why stable pointlike defects should exist. As discussed above, dissipation and restricted geometry may induce the formation of large alternating smectic regions. Tetratic domain walls in between these regions might form because of the density-depleted regions left behind by smectic domains. Another (indirect) reason may be the disparate curvatures of the outer and inner walls, which may limit the number of layers in a smectic region due to bend distortion (which would cause a nonuniform layer spacing along the radial direction), and ultimately control the number of regions in the sample. Their number is invariably equal to four in our experiments. This number may result from a balance between available space, difference in wall curvatures, and layer stiffness. Higher densities, more similar wall curvatures and possibly larger systems (not possible with our present experimental setup) might induce the formation of more smectic regions and/or different structures.

The presence of pointlike defects are more difficult to explain. Local tetratic fluctuations together with wall curvature could induce the formation of stable defects. In any case, despite the presence of the obstacle, which suppresses the long-range defect interaction along the cavity diameter, repulsive interactions between neighboring defects are probably quite strong since they are mediated by the rather stiff smectic layers.

As discussed in the Introduction, computer simulations based on equilibrium Monte Carlo methods have been useful to discuss the phenomenology of vibrated monolayers [23]. For the present annular systems, direct simulations of an equivalent system do not exist. Therefore, it would be interesting to analyze this system using equilibrium simulation techniques, which would help elucidate the role played by nonequilibrium effects or otherwise on the structures observed in granular monolayers. In this respect, simulations with dissipative or active-matter models that also incorporate interactions promoting orientational liquid-crystalline order might be useful.

Interestingly, Gârlea *et al.* [30] have observed similar structures in systems of virus particles confined into circular cavities and in annular cavities. Their system is different in that (i) virus particles have a high length to width ratio, meaning that their stable liquid-crystalline phase is a uniaxial nematic phase, and (ii) the ratio of inner and outer wall radii is larger. In this case, domains of nematic order with different orientation separated by domain walls are observed. Accompanying simulations that try to mimic the experimental system were also presented. In this case, structures with increasing numbers of domains are observed as the size of the central obstacle is increased and the two wall curvatures become more similar.

Even though the system explored by Gârlea *et al.* [30] is in a different range of length parameters, and the nature of the orientational ordering is simpler, the main result is qualitatively similar: the presence of ordered domains induced by reduced space and geometrical frustration of the order parameter. In our case, however, the structure of the domain walls seem to be far more complex, probably in part because of the larger variety of possible particle orderings (tetratic and smectic).

To summarize, we have presented results for the liquid-crystalline ordering exhibited by vibrated monolayers of granular rods when confined in circular and annular cavities. The circular cavity is analyzed as a reference case where topology should couple to ordering symmetry in a way totally different from that in annuli. Whereas topological arguments seem to apply for the circular cavity, in annuli we observe the formation of alternating smectic regions arranged azimuthally, separated by tetratic domain walls. Arguments based on dissipation and the stiffness of layered regions may help explain the formation of these structures in a qualitative way. But many questions remain open and deserve further research. In particular, the existence of pointlike defects with an orientationally disordered structure inside the domain walls cannot be explained, as there should be no symmetry conflicts in the annular geometry. The extent to which arguments based on elastic theory, which have been invoked in the past [22], can be applied in the present case is probably quite limited. The fine structure of steady-state configurations may stem from genuinely nonequilibrium effects in vibrated monolayers, with pointlike defects less prone to get unstable by the imposed annular symmetry than in equilibrium systems, or it may be simply the result of the different symmetry of the order parameter and the richer bulk phase diagram with more phases, one of them spatially nonuniform and favored by dissipation, competing in the same region.

The results presented in this paper present a theoretical challenge and future studies involving larger monolayers, including simulations of equivalent systems with and without dissipation, may give hints in this respect.

ACKNOWLEDGMENTS

Financial support under Grants No. FIS2017-86007-C3-1-P from Ministerio de Economía, Industria y Competitividad (MINECO) of Spain and No. PGC2018-096606-B-I00 from Agencia Estatal de Investigación-Ministerio de Ciencia e Innovación of Spain are acknowledged. We also gratefully acknowledge technical assistance by F. Borondo.

---

[1] Y.-H. Taguchi and H. Takayasu, Europhys. Lett. **30**, 499 (1995).
[2] D. R. M. Williams, Physica A **233**, 718 (1996).
[3] B. C. Eu and H. Farhat, Phys. Rev. E **55**, 4187 (1997).
[4] E. L. Grossman, T. Zhou, and E. Ben-Naim, Phys. Rev. E **55**, 4200 (1997).
[5] T. P. C. van Noije and M. H. Ernst, Granular Matter **1**, 57 (1998).
[6] E. Clement and J. Rajchenbach, Europhys. Lett. **16**, 133 (1991).
[7] S. Warr, G. T. H. Jacques, and J. M. Huntley, Powder Technol. **81**, 41 (1994).
[8] S. Warr, J. M. Huntley, and G. T. H. Jacques, Phys. Rev. E **52**, 5583 (1995).
[9] A. Kudrolli, M. Wolpert, and J. P. Gollub, Phys. Rev. Lett. **78**, 1383 (1997).
[10] J. S. Olafsen and J. S. Urbach, Phys. Rev. Lett. **95**, 098002 (2005).
[11] *Theory and Simulation of Hard-Sphere Fluids and Related Systems*, Lecture Notes Physics, Vol. 753, edited by A. Mulero (Springer, Berlin Heidelberg, 2008).
[12] R. P. Ojha, P.-A. Lemieux, P. K. Dixon, A. J. Liu, and D. J. Durian, Nature **427**, 521 (2004).
[13] F. Melo, P. Umbanhowar, and H. L. Swinney, Phys. Rev. Lett. **72**, 172 (1994).
[14] B. Miller, C. O'Hern, and R. P. Behringer, Phys. Rev. Lett. **77**, 3110 (1996).

[15] I. S. Aranson and L. S. Tsimring, Rev. Mod. Phys. **78**, 641 (2006).

[16] E. Khain and I. S. Aranson, Phys. Rev. E **84**, 031308 (2011).

[17] Y. Martínez-Ratón, E. Velasco, and L. Mederos, J. Chem. Phys. **125**, 014501 (2006).

[18] F. X. Villarruel, B. E. Lauderdale, D. M. Mueth, and H. M. Jaeger, Phys. Rev. E **61**, 6914 (2000).

[19] D. L. Blair, T. Neicu, and A. Kudrolli, Phys. Rev. E **67**, 031303 (2003).

[20] V. Narayan, N. Menon, and S. Ramaswamy, J. Stat. Mech.: Theory Exp. (2006) P01005.

[21] J. Galanis, D. Harries, D. L. Sackett, W. Losert, and R. Nossal, Phys. Rev. Lett. **96**, 028002 (2006).

[22] J. Galanis, R. Nossal, W. Losert, and D. Harries, Phys. Rev. Lett. **105**, 168001 (2010).

[23] T. Müller, D. de las Heras, I. Rehberg, and K. Huang, Phys. Rev. E **91**, 062207 (2015).

[24] M. González-Pinto, F. Borondo, Y. Martínez-Ratón, and E. Velasco, Soft Matter **13**, 2571 (2017).

[25] R. Blumenfeld and S. F. Edwards, Phys. Rev. Lett. **90**, 114303 (2003).

[26] S. F. Edwards, Physica A **353**, 114 (2005).

[27] M. González-Pinto, J. Renner, D. de las Heras, Y. Martínez-Ratón, and E. Velasco, New J. Phys. **21**, 033002 (2019).

[28] D. de las Heras and E. Velasco, Soft Matter **10**, 1758 (2014).

[29] M. J. Bowick and L. Giomi, Adv. Phys. **58**, 449 (2009).

[30] I. C. Gârlea, P. Mulder, J. Alvarado, O. Dammone, D. G. A. L. Aarts, M. P. Lettinga, G. H. Koenderink, and B. M. Mulder, Nat. Commun. **7**, 12112 (2016).